Materials & Design 244 (2024) 113146

Contents lists available at ScienceDirect

Materials & Design

journal homepage: www.elsevier.com/locate/matdes

Design of corrosion-resistant alloys for preventing oxidation-induced nanoscale Cr-depletion by inclusion engineering

K.P. Yu [a], H. Jiang [a], X.Y. Xu [a], M.X. Huang [a,*]

[a] Department of Mechanical Engineering, The University of Hong Kong, Pokfulam Road, Hong Kong, China

ARTICLE INFO

Keywords:
Cr-depletion
Corrosion-resistant
Inclusion engineering
Silicon
Aluminum
Titanium

ABSTRACT

Due to the preferential oxidation of Cr in various corrosion-resistant alloys, Cr-depletion extensively forms around the oxides and impairs passivation ability. This harmful effect has been widely recognized, but available solutions are limited. Here, to prevent such oxidation-induced Cr-depletion in corrosion-resistant alloys, we proposed a general strategy based on inclusion engineering using oxygen-preferred elements in alloy design. The inclusion-Cr depletion-passivation relationship was systematically studied in 3.5 wt% NaCl using commercially cast original, Si-modified, Al-modified, and Ti-modified CoCrFeMnNi alloys, in which the prominent inclusions were identified as $MnCr_2O_4$, MnO-SiO_2, AlN, and TiN, respectively. Unlike the original alloy, all modified alloys prevented Cr-depletion with improved corrosion resistance; however, the Si-modified alloy exhibited the most remarkable improvement due to few nitride by-products. Thermodynamic analysis on the free energy changes of potential reactions revealed that all the additives were preferential to be oxidized over Cr, whereas Al and Ti nitridation reactions have the most negative free energies compared to all oxidation reactions, which validated experimental results. From experiments and thermodynamics, an effective method was proposed, and its application was discussed with three newly-designed alloys prepared using arc melting. We believe the proposed strategy can be widely used in designing alloys to prevent oxidation-induced Cr-depletion.

1. Introduction

Chromium-based passivation was found in the early 1910s [1] and has always been the essential mechanism for extensive corrosion-resistant alloys, such as stainless steel [2,3], nickel-based alloys [4,5], which have been widely used in infrastructures and industrial equipment, and recently developed high entropy alloys (HEAs) [6–8]. To form a protective passive film in an alloy, sufficient Cr is required. For stainless steel, the critical threshold of Cr content was evaluated to be 11~13 wt% through experiments and simulations based on percolation theory [9–11]. However, local Cr-depletion frequently generates around inclusions in material preparation. Due to a decreased Cr concentration, sometimes falling severely below the critical threshold, passive films formed over these regions are known to be susceptible and, thus, preferential to induce local corrosion or passivation failure [12,13].

Despite some controversy, it has been suggested that Cr-depletion can be generated in the vicinity of sulfide inclusions [14–16], particularly MnS. In 316F stainless steel, for instance, a Cr-depletion band with 200–400 nm was observed around MnS [14]. One crucial explanation for the MnS-induced Cr-depletion is the substitution of chromium for manganese, which leads to the formation of more complex (Mn, Cr)-sulfides with high Cr content of 37 wt% [15] as well as lower Cr concentrations surrounding. It is argued that this Cr-depletion band dissolves ahead of MnS, thereby initiating pitting corrosion. On the other hand, the dissolution of MnS itself was believed to trigger pitting corrosion [17–19]. Consequently, sulfur content is often controlled to low levels in advanced alloys that require superior corrosion resistance.

Oxide inclusions often predominate over MnS in common stainless steels without re-sulfurization, as the oxidative atmosphere cannot be entirely prevented, particularly in industrial productions [20]. In addition to impurities associated with natural minerals, oxide inclusions can form in various metallurgical processes, such as solidification [21–23], high-temperature processing [24,25], and sprayed coating [12,26,27]. A typical example is the stainless steel prepared by thermal spraying [12]. Two major oxides of $FeCr_2O_3$ and $(Cr, Fe)_2O_3$ with a large amount of Cr formed at the intersplats. The oxidative reactions consumed the surrounding Cr and led to the formation of Cr-depletion near the intersplats during solidification or thermal processing. As a result, the Cr: Fe ratio in

* Corresponding author.
E-mail address: mxhuang@hku.hk (M.X. Huang).

https://doi.org/10.1016/j.matdes.2024.113146
Received 26 April 2024; Received in revised form 22 June 2024; Accepted 7 July 2024
Available online 8 July 2024

the edge of the steel to inclusion is ~0.27, quite lower than ~0.37 in the distant matrix, not to mention those in the oxides. Pitting corrosion was frequently found in this susceptible area due to the galvanic cells between the Cr-depletion regions and Cr-rich oxides. Furthermore, increasing when Mn-alloying increased, corrosion resistance appeared to degrade more severely [28–30]. For instance, increasing Mn content in a Fe-18Cr casted alloy [27] led to more frequent pitting, even at the sites without MnS. Before pitting propagation, the electrochemical current spiked at higher magnitudes in the metastable region. This deterioration was attributed to the increase in the density and size of (Fe, Cr, Mn)-oxides, which enhanced the probability of pitting initiation. More seriously, in a CoCrFeMnNi casted alloy with ~20 wt% Mn, no passivation behavior was observed during potentiodynamic polarization in 3.5 wt% NaCl [13,31]. Localized corrosion occurred from the edge of the matrix to the $MnCr_2O_4$ inclusion, where the Cr content was lower to ~13 wt% [13], nearing the critical point for passivation. The increased Mn content may exacerbate Cr-depletion by facilitating oxidative reactions, as spinel oxide forms from corundum oxide released heat, which was thermodynamically favored [21].

Although the harmful effect of oxidation-induced Cr-depletion on corrosion resistance has been widely investigated, solutions to address this issue remain limited. One direct method is to reduce atmospheric oxygen levels. For instance, the CoCrFeMnNi alloy made using a high vacuum arc furnace demonstrated greater pitting resistance than its non-passive counterpart produced with common melting equipment, owing to a lower density of oxides under higher vacuum degrees [13]. However, implementing high vacuum conditions is costly and challenging in large-scale industrial production. Another possible method is to minimize inclusion density by surface treatments, like acid cleaning. In this case, inclusions, as well as the susceptible Cr-depletion regions near the surface, were probably to be removed [32–35]. While this method can sometimes be effective as the surface is cleaned comprehensively, the inner Cr-depletion may still be exposed when suffering from mechanical abrasion in real-world applications.

In ferrous process metallurgy, inclusion engineering has been proposed to achieve deoxidation by thermodynamically adjusting the composition and structure of inclusions in addition to their size and density [36–38]. Previous research implied that such inclusion modification [13] could be a practical method for improving corrosion resistance, but it is fragmentary, and the mechanism attached to anti-corrosion enhancement was not fully understood. As various Cr-containing oxides, such as Cr_2O_3 [39], $MnCr_2O_4$ [23,29], $FeCr_2O_4$ [12], (Cr, Mn)(O, C, S) [40], (Cr, Mn, Al)O [41], $(Co_x, Ni_{1-x})Cr_2O_4$ [27] were found in alloys fabricated by different metallurgical techniques, they probably follow different mechanisms and formation pathways, making the issue somewhat complicate. In the present study, we propose an effective strategy based on inclusion engineering, specially tailored to avoid oxidation-induced Cr-depletion in alloy design. This strategy was accomplished after a systematical and detailed investigation of the original, Si-modified, Al-modified, and Ti-modified CoCrFeMnNi high entropy alloys, in which the inclusions and surrounding Cr distributions were studied by transmission electron microscopy (TEM), energy dispersive spectroscopy (EDS), and energy electron loss spectroscopy (EELS), and corrosion resistance was measured by potentiodynamic polarization (PDP). The underlying mechanism was elucidated by thermodynamic analysis, and its application was discussed using three newly-developed alloys.

2. Materials and methods

2.1. Materials

Four alloys were used for the initial study, including the original, Si-modified, Al-modified, and Ti-modified CoCrFeMnNi HEAs. In addition, another three alloys were developed to validate the proposed strategy, including Ni-20Cr20Mn, Ni-20Cr20Mn2Si, and V-20Cr20Mn in nominal weight percentage. Fig. 1a shows the preparation steps of the four HEAs, in which all raw materials used were commercially available pure elements, not highly purified, and the metallurgical processes were under moderate vacuum conditions. The present alloy preparation indicates that inclusions are inevitably present in all HEAs. The chemical compositions of the four HEAs are shown in Table 1. The contents of Co, Cr, Fe, Mn, Ni, Si, Al, and Ti were measured using an inductively coupled plasma-optical emission spectrometer (ICP-OES, Agilent 5100). The contents of O, S, and N were determined using a gas analyzer (LECO CS206 and ON836).

2.2. Characterizations

The HEA phases were determined using X-ray diffraction (XRD, Rigaku, SmartLab) with Cu Kα radiation over a 2θ range of 35~100° and were analyzed with the ICCD database (PDF#03-065-9094 and PDF#00-004-0850). The inclusions in all HEAs were first analyzed using scanning electron microscopy (SEM) equipped with an energy dispersive spectroscopy (EDS) detector and electron back-scattering diffraction detector (EBSD). Inclusion area ratios were roughly evaluated by ten SEM images using ImageJ software, respectively. Inclusion cross-sections were prepared by a lift-out method using a focused ion beam (FIB), and their structures with nearby elemental distributions were analyzed using a transmission electron microscopy (TEM, Talos F200X) equipped with Super-X EDS detector and electron energy loss spectroscopy (EELS). Thermodynamic calculations were based on the proposed reactions using the HSC chemistry database.

2.3. Electrochemical measurements

To evaluate the passivation behaviors for all HEAs, potentiodynamic polarization (PDP) was carried out in an aerate 3.5 wt% NaCl solution at room temperature using an electrochemical workstation (PARSTAT 3000A, Princeton Applied Research). A three-electrode cell was employed, and the samples, a saturated calomel (SCE) and Pt sheet served as the working electrode, reference electrode, and counter electrode, respectively. The tested HEAs were machined in a 10 × 10 × 3 mm^3 dimension and molded by epoxy resin with one face (10 × 10 mm^2) exposed. Note that all the tested alloys were treated in 30 vol% HNO_3 at 50 °C for 60 mins before molding to avoid the influence of crevice corrosion [42]. Moreover, the absence of crevice corrosion was confirmed after each corrosion test using optical microscopy, as in previous research [13]. The exposed faces were ground to 2000 grit with SiC papers and cleaned using acetone and deionized water. Before testing, the samples were polarized at −0.85 V_{SCE} for 5 min to remove the air-formed passive film and retained in the solution for 1 h to obtain a relatively stable open circuit potential (OCP). The PDP measurements were conducted at a scanning rate of 0.33 mV/s.

3. Results

3.1. Macroscopic observations

The original CoCrFeMnNi and the other three modified CoCrFeMnNi alloys, namely O-HEA, Si-HEA, Al-HEA, and Ti-HEA, are considered in this study. First, the water-quenched samples (Fig. 1a) were ground and polished to expose inner inclusions, followed by structural and morphological characterizations using XRD and SEM. The XRD results in Fig. 1b show that O-HEA, Si-HEA, and Al-HEA have a full FCC structure, whereas Ti-HEA, despite having the same FCC matrix, seems to contain a certain amount of the other phases (see the dashed square). According to PDF cards, this new phase is primarily identified as Ti nitrides, which will be disclosed in the following sections. Surface morphologies (Fig. 2a) indicate the presence of inclusions in all alloys, whereas the inclusion amount of Ti-HEA is significantly higher compared to the other alloys. To roughly quantify inclusions, a statistical analysis of the

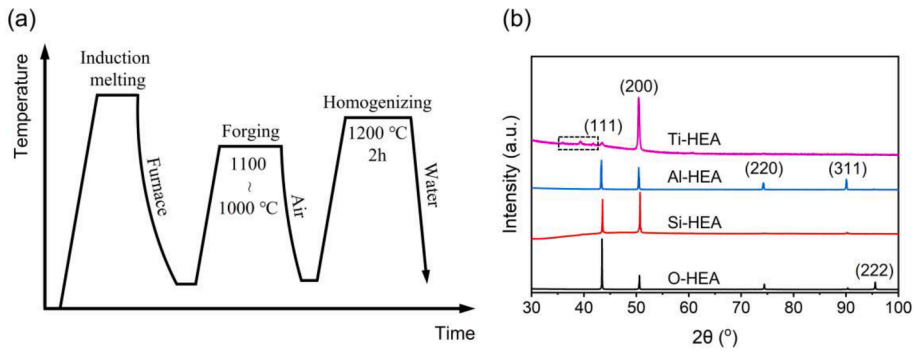

Fig. 1. Material preparation and structures. (a) A schematic illustration of metallurgical and thermomechanical processing of the four HEAs. (b) XRD spectra of the four HEAs after homogenization.

Table 1
Chemical compositions of O-HEA, Si-HEA, Al-HEA, and Ti-HEA in the present study. X represents Si, Al, and Ti in Si-HEA, Al-HEA, and Ti-HEA, respectively.

Alloys		Co	Cr	Fe	Mn	Ni	S	X
O-HEA	wt.%	21.5	18.3	21.0	19.6	19.5	0.0097	–
	at.%	20.4	19.8	21.0	20.0	18.6	0.017	–
Si-HEA	wt.%	21.0	19.0	20.1	18.8	19.3	0.0088	1.76
	at.%	19.6	20.1	19.8	18.9	18.1	0.0150	3.35
Al-HEA	wt.%	19.5	19.3	19.5	20.0	19.6	0.0047	2.00
	at.%	18.1	20.4	19.1	19.9	18.3	0.0080	4.05
Ti-HEA	wt.%	19.4	19.8	20.2	20.0	18.8	0.0054	1.82
	at.%	18.3	21.2	20.2	20.3	17.8	0.0090	2.12

inclusion area ratio based on ten images at 500x magnification was conducted. The results (Fig. 2b) show that the inclusion area ratio in Ti-HEA is as high as 3.01 %, far more than those in the other HEAs, which provides a sufficient signal for XRD detection by a common source (Fig. 1b).

Fig. 3 shows the SEM-EDS results of the typical inclusions in the four HEAs. It can be observed that MnS presents in all the samples, as widely recognized [43]. Compared to O-HEA from EDS mapping results, the inclusions in Si-HEA, Al-HEA, and Ti-HEA form primarily due to the addition of Si, Al, and Ti, respectively. Notably, regardless of the element introduced, Cr is no longer enriched in the inclusions (including MnS) of the modified CoCrFeMnNi alloys. One significant difference between the modified HEAs is that the Si-HEA inclusions are oxides, whereas the inclusions in both Ti-HEA and Si-HEA are nitrides. These observations align well with the quantitative measurements of O and N for the bulk alloys (Fig. 2b).

3.2. Inclusion microstructures

To unveil their microstructures and compositions, we lifted out typical inclusions using FIB and then analyzed them using TEM, EDS, and EELS. Although MnS is commonly present in all the HEAs, nearly no Cr is incorporated, as revealed by SEM-EDS (Fig. 3). For simplifying and focusing on oxides, MnS will not be specifically identified. Thus, the inclusions in the following sections are referred to as Cr-based, Si-based, Al-based, and Ti-based oxides/nitrides in O-HEA, Si-HEA, Al-HEA, and Ti-HEA, respectively.

3.2.1. O-HEA inclusion identification by TEM-EDS

We first identified the inclusion in O-HEA, as shown in Fig. 4. The HAADF image in Fig. 4a presents an overall view. It can be determined from the high-resolution TEM (HRTEM) image and corresponding fast Fourier transformation (FFT) patterns (Fig. 4b) that the inclusion has a face-centered cubic (FCC) structure. Moreover, STEM-EDS (Fig. 4c) shows that the inclusion is rich in Cr, Mn, and O but deficient in Fe, Ni, and Co. Combining the EDS point spectrum (Fig. S1a), the chemical formula of Cr-rich oxide is finally determined to be $MnCr_2O_4$ with a lattice parameter a = 8.47 Å (PDF# 00-054-0876), which has also been reported in previous studies [13,31]. In contrast to the Cr chemical composition of ~20 wt% in the matrix, the Cr content in $MnCr_2O_4$ is as high as 27.6 wt%, indicating the diffusion of Cr from the matrix [12].

3.2.2. Si-HEA inclusion identification by TEM-EDS

Fig. 5a is the HAADF image showing a part of the inclusion in Si-HEA. One can see that after adding Si, the inclusion is transformed into amorphous, as supported by the HRTEM image (Fig. 5b) and corresponding FFT diffractogram (Fig. 5c). Further EDS elemental mapping reveals that the inclusion is no longer rich in Cr but comprises both the newly introduced Si and Mn. Although the point spectra (Fig. S1b) cannot determine the atomic ratio of Mn: Si: O, the amorphous oxide has been widely found in steel. This oxide family is commonly named MnO-SiO_2 [44,45], as is the case in the present study.

3.2.3. Al-HEA inclusion identification by TEM-EDS-EELS

Fig. 6a shows the FIB thin foil inside with two separated Al-HEA inclusions. The inclusion-matrix interface was examined using TEM and STEM-EDS, as shown in Fig. 3b-d and Fig. 3f-h. From the selected area electron diffraction (SAED) diffractogram (insert image in Fig. 6d), the matrix structure is identified as FCC, which is consistent with XRD spectra (Fig. 1b). Meanwhile, HRTEM with the corresponding FFT diffractogram and standard atom model (Fig. 6f-h) reveals that the AlN has a hexagonal close-packed structure (HCP). The EDS mapping images (Fig. 6c) show that the modified inclusions only contain Al and N, with almost no Cr. Same elemental distributions are also identified by EELS mapping, and no other light elements, such as C and O, are incorporated (Fig. S2). Since the EDS point spectrum is accurate enough (Fig. S1c), EELS was used for quantifying. As shown in Fig. 6e, the count ratio of Al and N in the inclusion is finally quantified as one-to-one, revealing a chemical formula of AlN. Hence, the inclusion in Al-HEA is determined to be HCP AlN (PDF#01-075-1620), and the corresponding lattice parameter is a = 3.13 Å (Fig. 6f).

3.2.4. Ti-HEA inclusion identification by TEM-EELS

The microstructure identification of Ti-based inclusion in Ti-HEA by TEM-EELS is shown in Figs. 7 and 8. Since EDS spectra of light elements such as N, O, and C are hidden in the spectra of other major elements, particularly Ti (Fig. S1d), it is difficult to outline their locations and even make a qualitative analysis (Fig. S3); thus, EELS elemental mapping was used instead of EDS. As shown in Fig. 8b, the EELS elemental mapping demonstrates different distributions of light elements compared with EDS (Fig. S3). The spectra determine that the anions in the Ti-based

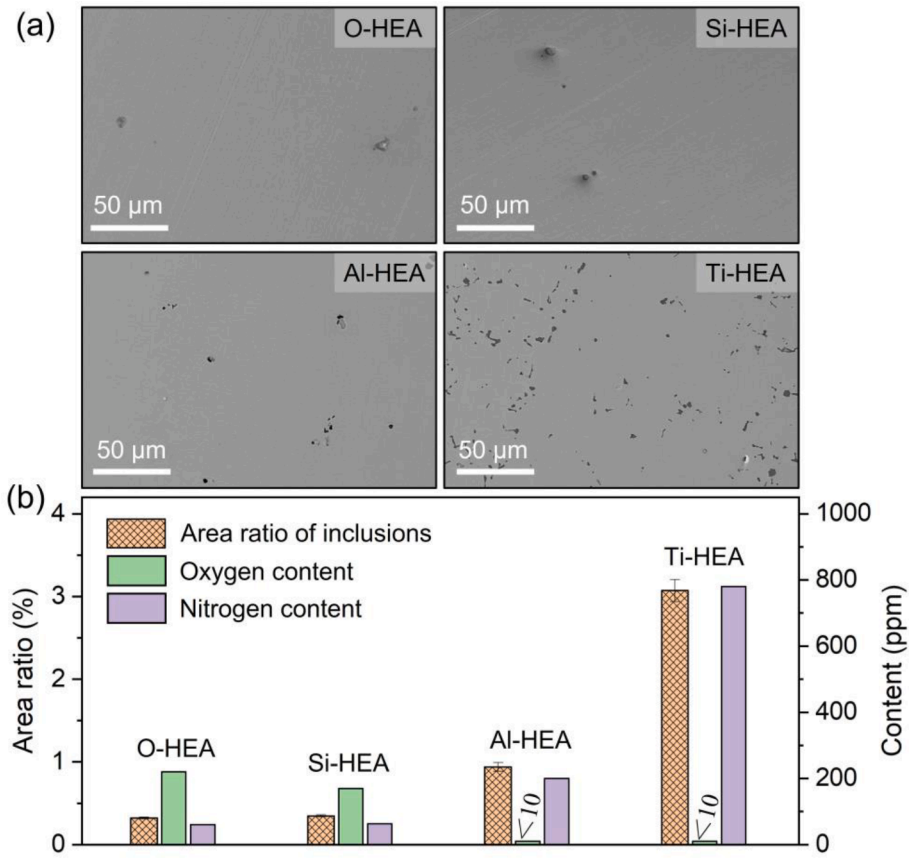

Fig. 2. Inclusion analysis of the four HEA alloys. (a) SEM images of the inclusions in O-HEA, Si-HEA, Al-HEA, and Ti-HEA, respectively. (b) Characterizations on inclusion area ratios and the contents of O and N in HEAs.

inclusions are a mixture of N, O, and C.

The representative background-subtracted EELS core-loss spectra of the area outlined in Fig. 7a were extracted and presented in Fig. 7e. By comparison, the peaks of C are observed in all selected regions, whereas O and N are present in the core of the inclusion. This is reasonable given that both TiC and TiN have an FCC structure, as revealed by Fig. 7c-d. Some unknown spots (yellow arrows) are also observed in square *d* according to the FFT diffractograms in Fig. 7d2. On the other hand, the chemical composition measure from the EELS line-scanning corresponds well to the chemical assembly of TiC, TiN, and TiO_2 (Fig. 8c), indicating the unknown spots may originate from TiO_2 diffraction. Note that TiC may be an impurity already present in the raw materials, and TiO_2 may be a by-product of exposing FIB foil to the air. However, the majority of Ti-based inclusions should be TiN [46,47], as supported by the overall measurements of O and N contents (Fig. 2b). The oxygen content in Ti-HEA is below 10 ppm, whereas the nitrogen content is as high as 800 ppm. Hence, the inclusions in Al-HEA are mostly composed of FCC TiN (PDF#00-002-1159), slight impurities of TiC, and perhaps tiny Ti-contained oxides. The lattice parameter of the major FCC TiN is identified as a = 4.48 Å (Fig. 7c and d).

3.2.5. *Inclusion confirmation by EBSD*

According to inclusion identification, i.e., cell structure and lattice parameters, crystal files of $MnCr_2O_4$, TiN, AlN, and MnS were built for EBSD analysis. Subsequently, large-scale inclusion confirmation was conducted with EDS to differentiate phases with similar structures but different chemical compositions. Fig. 9 gives some representative results. The band maps (Fig. 9a-d) clearly locate the inclusions in different HEAs where TiN is most prevalent in both grains and grain boundaries. Meanwhile, the detected Kikuchi patterns of $MnCr_2O_4$ (green pixels in Fig. 9e), amorphous MnO-SiO_2 (dark pixels in Fig. 9f), AlN (blue pixels in Fig. 9g), and TiN (pink pixels in Fig. 9h) match well with the standard Kikuchi lines of the edges extracted from database, respectively. Note that the brown pixels represent some Al-based oxides as impurities. The EBSD results confirm the structure identifications from TEM and the extensive formation of $MnCr_2O_4$, MnO-SiO_2, TiN, and AlN in O-HEA, Si-HEA, TiN, and AlN, respectively.

3.3. *Cr distributions*

Due to its crucial role in corrosion resistance [2,4,8], Cr distributions across the inclusion-matrix interfaces were specially analyzed using EDS elemental line-scanning. The corresponding HAADF images were extracted with line profiles, where the inclusions are on the left and the matrixes are on the right. Fig. 10a shows the elemental line profile of the inclusion-matrix interface in O-HEA. The valley-shaped HAADF profile across the interface indicates the presence of a gap that might be occupied by MnS or nano-particles milled during FIB foil preparation. Interestingly, the results show that all the principal elements have concentrations that are similar to those far from the interface. i.e., at the position of 600 nm, indicating a homogenous distribution (Fig. 10a). However, the closer to the interface, the more depleted the Cr concentration is, which is different from those of Fe and Co with no diffusion. The Cr-depletion zone is estimated to be 150–200 nm, and the Cr concentration at the interface is only ~10 wt%. Such an area is often believed to be the region prone to induce pitting corrosion and passivation failure [12–14,26,48]. It is worth noting that the sharp decreases of all the elements in the gray regions are due to the overlap between the matrix and inclusion from the observed direction, which can be revealed by HAADF profiles. After adding Si, Al, and Ti, in sharp contrast, the decreased tendency of Cr concentration is no longer present (Fig. 10b-d) since Cr is nearly absent in oxides of Si-HEA and nitrides of Al-HEA and

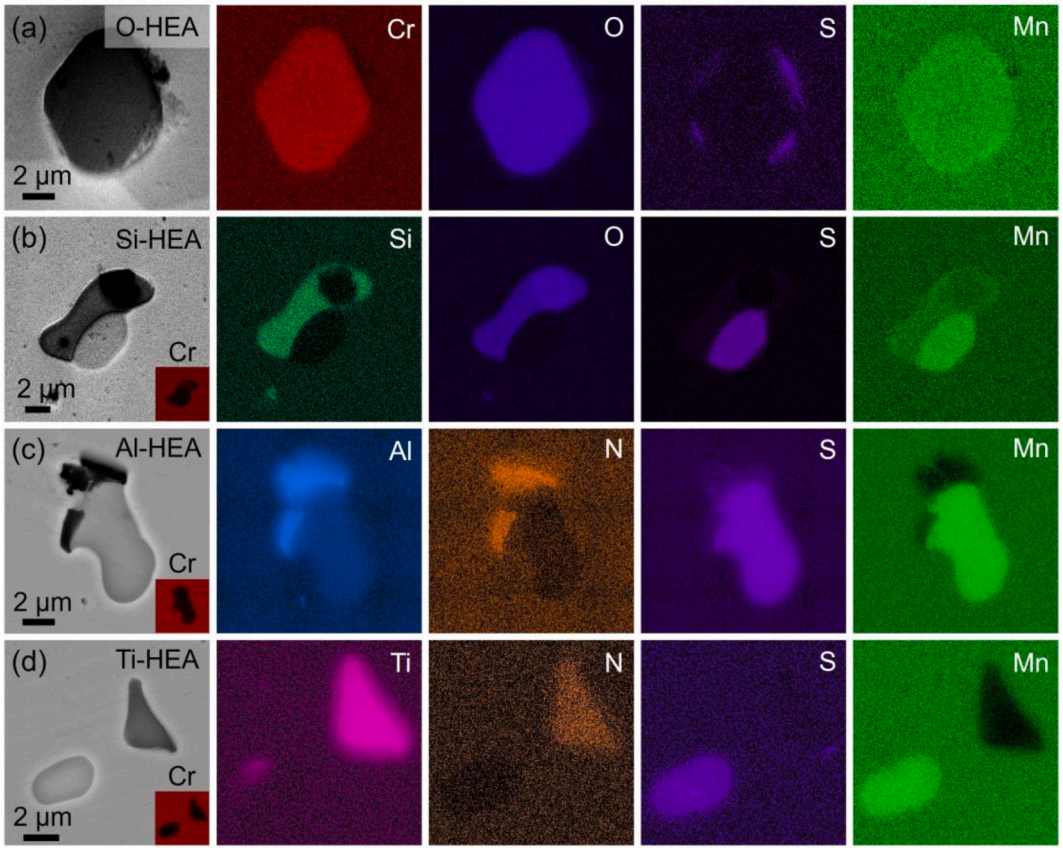

Fig. 3. SEM-EDS mapping of the inclusions in the four alloys. (a) O-HEA. (b) Si-HEA. (c) Al-HEA. (d) Ti-HEA.

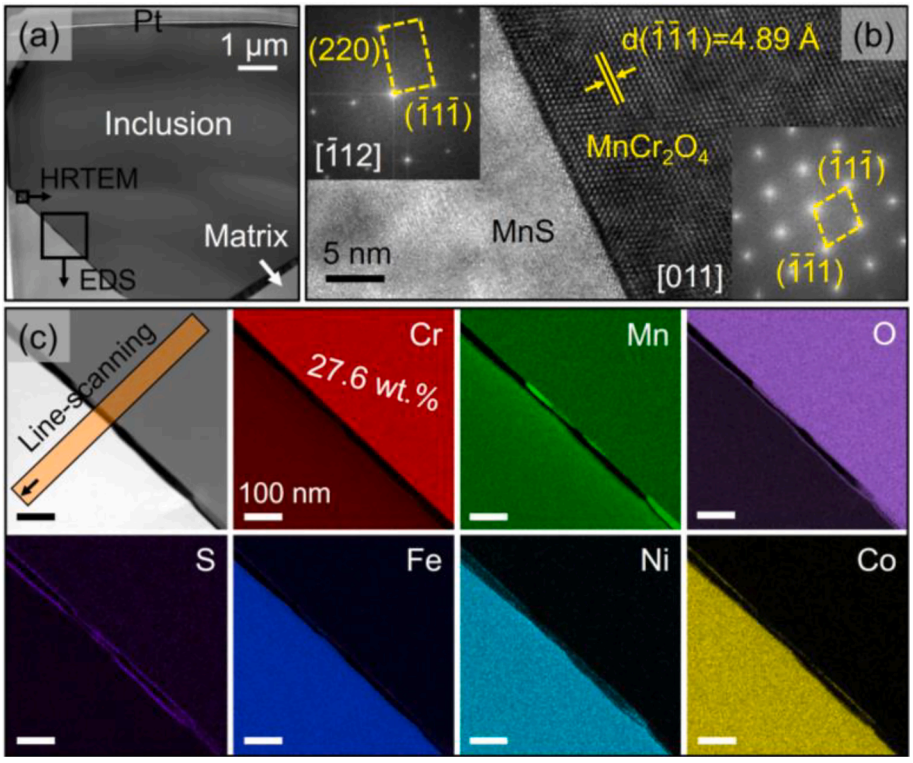

Fig. 4. Identification of the inclusion in O-HEA. (a) HAADF image of the inclusion. (b) HRTEM image of the $MnCr_2O_4$-MnS interface outlined in (a). (c) EDS mapping of the area outlined in (a).

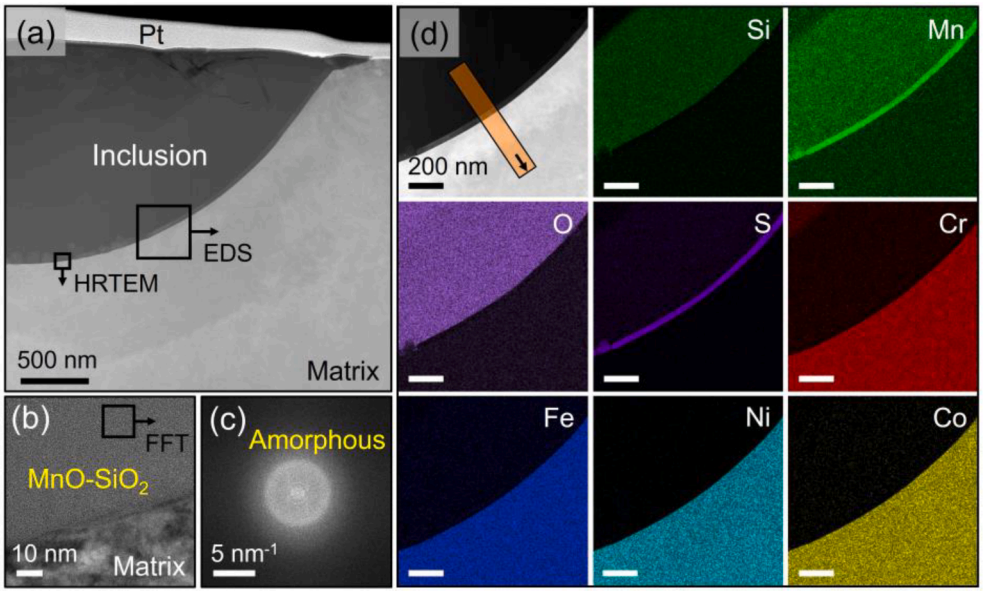

Fig. 5. Identification of the inclusion in Si-HEA. (a) HAADF image of the inclusion. (b) HRTEM image of the oxide-matrix interface outlined in (a). (c) FFT diffractograms of the MnO-SiO_2 inclusion. (d) EDS mapping of the area outlined in (a).

Ti-HEA (Fig. S1). In the meantime, due to an extremely low concentration of oxygen (<10 ppm) detected (Fig. 2b), it is believed that almost no $MnCr_2O_4$ or other Cr-based oxides formed in both Al-HEA and Ti-HEA. Hence, although the inclusions in Si-HEA, Al-HEA, and Ti-HEA are different, the nanoscale Cr-depletion is prevented by modifying inclusions.

3.4. Passivation behaviors

Next, the corrosion-resistant behavior of all HEAs was measured five times in 3.5 wt% NaCl using PDP. Fig. 11 shows all the experimental curves with a summary of corrosion current density (I_{corr}) and pitting potential (E_p). The fitting results of the Tafel region show that the average I_{corr} values of O-HEA, Si-HEA, Al-HEA, and Ti-HEA are 110, 58, 101, and 149 nA/cm^2, respectively. The larger fluctuations of I_{corr} and corrosion potential (E_{corr}) in Al-HEA and Ti-HEA are probably attributed to the more micro-galvanic cells formed between the matrix and inclusions (Fig. 2). However, the most significant observation is the passivation behavior, where O-HEA surprisingly demonstrates passivation failure. For clearer comparison, pitting corrosion in alloys with or without passivation behavior is assumed to occur at a current density of 100 μA/cm^2 [42]. As shown in Fig. 11, the average E_p values of O-HEA, Si-HEA, Al-HEA, and Ti-HEA are 56, 374, 203, and 118 mV, respectively. It indicates that all the doping elements improve the pitting resistance of CoCrFeMnNi, and the improvements from additives can be summarized as: Si > Al > Ti.

4. Discussion

4.1. Significance of Cr-depletion prevention

The passivation failure of the CoCrFeMnNi alloy in the NaCl solution has been acknowledged in previous studies, yet its underlying reasons appear to be diverse and complex [29,31,49]. One such cause is galvanic corrosion between the matrix and oxide inclusion. Pitting corrosion previously identified around the oxides was attributed to the formation of $MnCr_2O_4$/matrix galvanic cells. This argument gained support from the enhanced pitting resistance, which was achieved by reducing the volume of oxides in the matrix using high vacuum metallurgy techniques [31]. Another investigation attributed this severe deterioration to the presence of Mn and Co in the alloy. During PDP, Mn and Co just dissolved into cations, but corresponding oxides and hydroxides could not deposit due to the high H^+ concentration resulting from metal hydrolysis [49]. One proposed solution was to consume H^+ ions and increase local pH by alloying with N, thereby recovering the deposition of Mn and Co cations. It is worth noting that while pitting corrosion is commonly believed to commence with the dissolution of MnS in stainless steel [17–19], this does not necessarily mean passivation cannot occur in 3.5 wt% NaCl that is frequently observed in the CoCrFeMnNi alloy and importantly, the S content in O-HEA is relatively low (Table 1).

In contrast, our study emphasizes the fatal role of Cr-depletion in passivation failure. While Cr is well-known for its essential contribution to corrosion resistance, achieving effective passivation in alloys necessitates a specific chromium content, typically falling within the range of 11 to 13 wt% in stainless steel [9–11]. The passivation failure in O-HEA seems quite unusual in terms of a considerable amount of Cr, i.e., 20 wt %,. However, the EDS line-scanning across the oxide-matrix interface shows that Cr concentration near the matrix edge to oxide can lower to 10 wt% (Fig. 10a), of which the value is below its critical threshold. If localized corrosion prior forms in some sites [12,13] with such low Cr concentrations, the passivation of O-HEA as a whole becomes incomplete. This is why the I_{corr} of O-HEA in all repeated experiments (Fig. S4a) progressively increases without displaying a platform as the potential increases.

After Si addition, the alloy displays clear passivation regions and high pitting potentials in the range of 300~400 mV (Fig. 11), of which the level is comparable to commercial 316 stainless steel and other HEAs with similar pitting resistance equivalent numbers (PRENs). In other words, it signifies a “returning to its expected position” [50–53]. Although pitting corrosion can be found in both O-HEA and Si-HEA, pitting initiation was different (Fig. 12), as argued in our previous research [13]. Typically, O-HEA exhibits obvious pits (Fig. 12a) at 200 mV with the current density reaching ~1 mA/cm^2 (Fig. 11a), similar to the value observed when corrosion tests are halted. In contrast, the current density of Si-HEA at 200 mV ranges only from 10^{-4} to 10^{-2} mA/cm^2 with a metastable stage (Fig. 11b). Meanwhile, the concentrations of S associated with inclusions are often undetected (Fig. 12b). Therefore, we attribute this metastability to the dissolution of MnS. In addition to the improved corrosion resistance, Si-HEA exhibits both higher strength and ductility over O-HEA (Fig. S4), demonstrating the strong potential of Si to overcome the strength-ductility trade-off in HEAs. The mechanisms have been extensively studied, with the main reasons

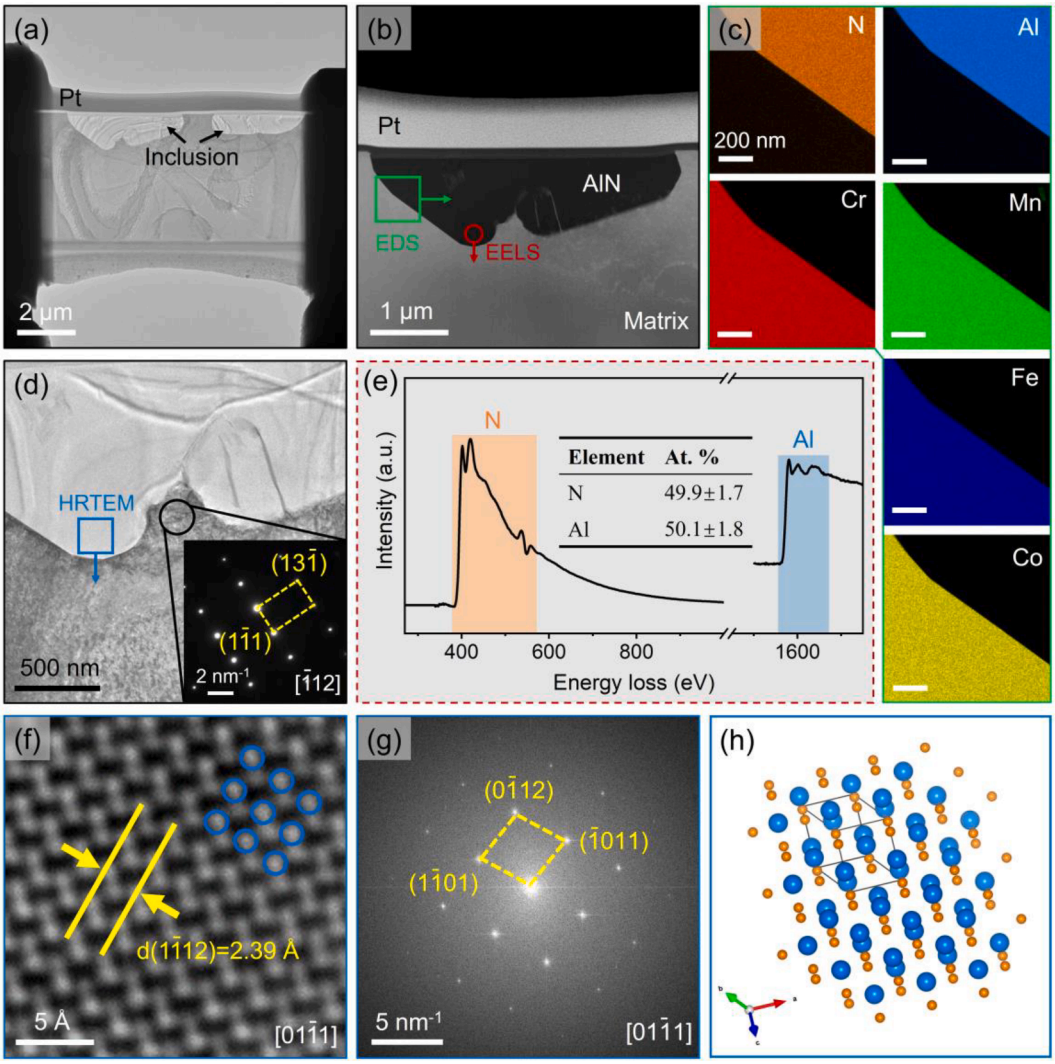

Fig. 6. Identification of the inclusion in Al-HEA. (a) TEM image of the sample prepared by FIB. (b) HAADF image of the inclusion. (c) EDS mapping of the area outlined by the green square in (b). (d) TEM image of the inclusion. (e) EELS point spectrum of the area outlined by the red circle in (b). (f) HRTEM image of the inclusion. (g) FFT diffractogram of the inclusion. (h) Standard atom model of AlN. (For interpretation of the references to colour in this figure legend, the reader is referred to the web version of this article.)

identified as the lower stacking fault energy and solid solution strengthening caused by Si addition [54–57]. Consequently, the current study focuses on the impact of corrosion resistance.

For the Al-HEA and Ti-HEA, although the oxides and Cr-depletion in the inclusion-matrix interface were effectively prevented (Fig. 2b and Fig. 10), these modifications generated more nitrides by-products (Fig. 2b, Fig. 6, and Fig. 7). Rather than the Cr-depletion region in O-HEA, pitting corrosion is more likely to occur in the matrix where MnS is assumed to be incorporated (Fig. 12c-d) and in the inclusion-matrix interfaces that more extensively present in Al-HEA and Ti-HEA. The increased quantity of inclusions can be observed from the statistical analysis of the inclusion area. The inclusion area ratios in O-HEA and Si-HEA are 0.32 % and 0.34 %, respectively, whereas in Al-HEA and Ti-HEA, they are 0.94 % and 3.01 %, respectively. The massive inclusions may also form galvanic cells with the matrix, potentially accelerating localized corrosion due to the larger anode-to-cathode area ratios. These reasons facilitate pitting initiation [51,58–60] and result in inferior improvement compared to Si-HEA. Particularly in Ti-HEA, given that the TiN precipitates are non-uniformly distributed in both grain and boundaries (Fig. 2a and 9), and the morphology of the bulk TiN inclusions varies [61], it is reasonable to expect Ti-HEA that have unstable performances (Fig. 11d). However, the comparison on pitting potentials (Fig. 11) reveals that Al and Ti somehow improve pitting resistance even when larger quantities of inclusions have been introduced.

Admittedly, fully understanding the mechanism of pitting corrosion and developing effective strategies is complicated, with variables such as the chemical compositions of passive films also likely being influenced by additives. Our focus is on the inclusion-Cr depletion-passivation relationship, as this is fundamentally related to the passivation of Cr-based alloys rather than the effects of passive film from minor additives. Moreover, these additives significantly affect the local environments of inclusion-matrix interfaces and the distribution of Cr. On this basis, the superior performance of Si-HEA over Al-HEA and Ti-HEA can be explained by two factors. First, the addition of Si prevents the formation of Cr-depletion zones, which are the most vulnerable to pitting corrosion. Second, unlike Al-HEA and Ti-HEA, Si-HEA generates significantly fewer inclusions (Fig. 2), thereby reducing the corrosion risk associated with the second phase and galvanic effect. In summary, we attribute the poor corrosion resistance of O-HEA to Cr-depletion and underscore the great importance of preventing its formation. Among these elements, Si not only enhances corrosion resistance most effectively but also successfully overcomes the strength-ductility trade-off.

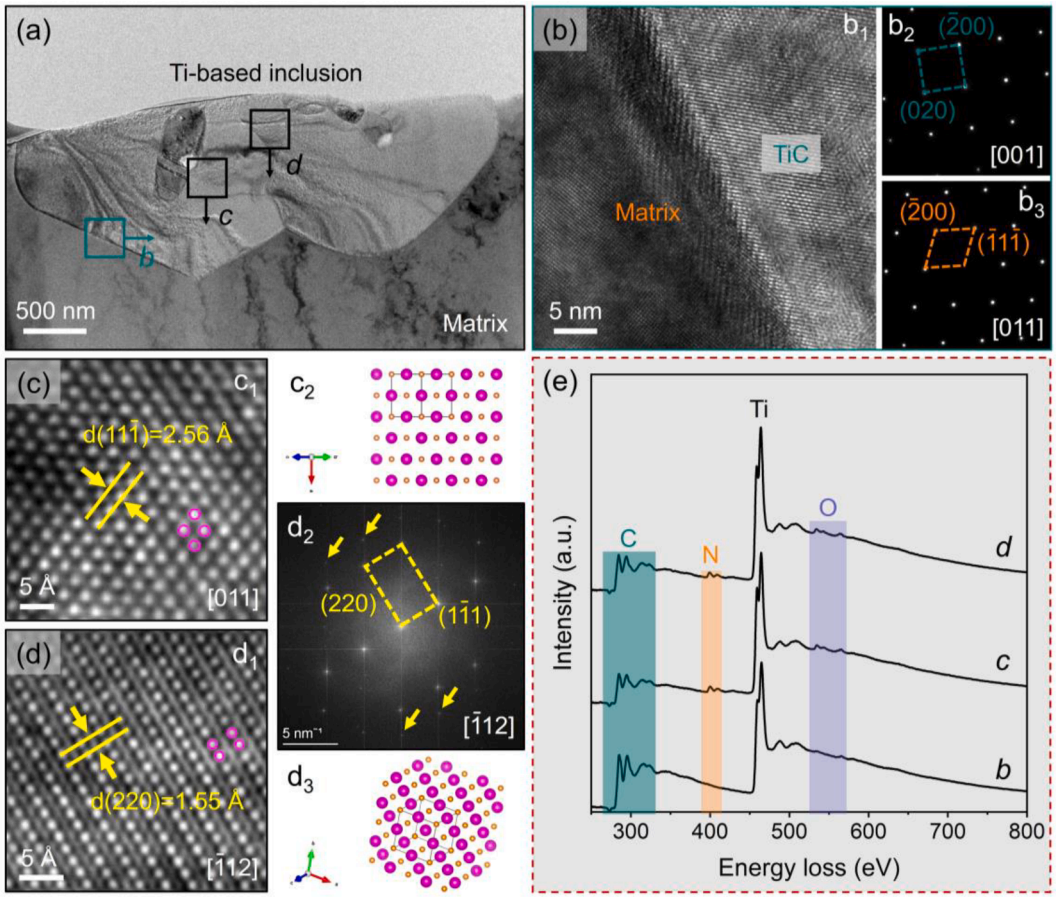

Fig. 7. Inclusion identification of the inclusion in Ti-HEA. (a) TEM image of the inclusion in Al-HEA. (b) Structure identification of the interface outlined by the square *b*. b_1: HRTEM image, b_2: SAED diffractogram of TiC, and b_3: SAED diffractogram of matrix. (c) Structure identification of the area outlined by square *b* in (a). c_1: HRTEM image, and c_2: standard atom model of TiN projected from [0 1 1]. (d) Structure identification of the area outlined by the square *d* in (a). d_1: HRTEM image, d_2: FFT diffractograms, and d_3: standard atom model of TiN projected from [1 1 2]. (e) EELS spectra of the area outlined by the squares *a*, and *d* in (a).

4.2. Thermodynamic basis of Cr-depletion prevention

Oxide inclusions of the alloys are inevitable in metallurgical processes and often come from two sources [20]. One is the endogenous inclusions resulting from reactions between metals and dissolved oxygen. The other is the exogenous inclusions caused by entrapping external sources. As described in the experimental procedures, the preparation of HEAs can be complicated, including several metallurgical techniques. However, unveiling the evolution of oxide inclusions step by step in different processes is challenging and might not be necessary. Rather than tracing intermediate products and local concentrations of each element, we focus on the thermodynamics of related chemical reactions subjected to moderate vacuum conditions in alloy preparation (Fig. 1a).

Consider a representative reaction of metals and gases:

$$xM + G_2 \rightarrow M_xG_2 \tag{1}$$

where M is metal, and G_2 represents the O_2 or N_2 gas considered in the present study. The Gibbs free energy change of the reaction can be given:

$$\Delta G = \Delta G_f + RTln\left(\frac{a_{M_xG_2}}{a_M^x \cdot p_{G_2}}\right) \tag{2}$$

where R is the gas constant, T is the absolute temperature, $a_{M_xG_2}$ is the chemical activity of the product, a_M is the activity of metal, and p_{G_2} is the partial pressure of the gas. At the equilibrium state, the free energy change for the reaction is equal to zero:

$$\Delta G_f = -RTln\left(\frac{a_{M_xG_2}}{a_M \cdot p_{G_2}}\right) \tag{3}$$

ΔG_f is formation energy that can be obtained from:

$$\Delta G_f = \Delta H^0_{298} - T\Delta S^0_{298} \tag{4}$$

where ΔH^0_{298} and ΔS^0_{298} is the standard enthalpy and entropy changes of corresponding oxide formation at 298 K. Provided one mole O_2 as a reference, the Gibbs formation energies of the proposed oxidation reactions can be calculated according to Eqs. (5)–(13).

$$2Ni + O_2 = 2NiO \tag{5}$$

$$2Co + O_2 = 2CoO \tag{6}$$

$$2Fe + O_2 = 2FeO \tag{7}$$

$$2Mn + O_2 = 2MnO \tag{8}$$

$$\frac{4}{3}Cr + O_2 = \frac{2}{3}Cr_2O_3 \tag{9}$$

$$\frac{1}{2}MnO + \frac{1}{2}Cr_2O_3 = \frac{1}{2}MnCr_2O_4 \tag{10}$$

$$Si + O_2 = SiO_2 \tag{11}$$

$$Ti + O_2 = TiO_2 \tag{12}$$

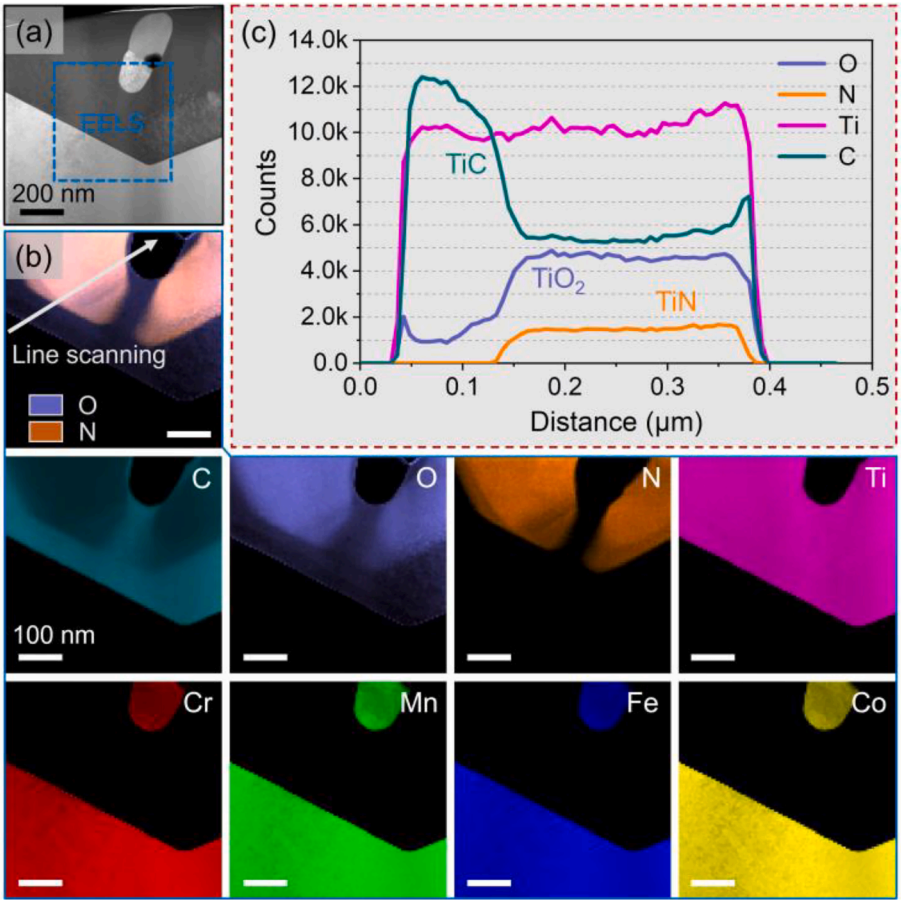

Fig. 8. EELS spectra of the inclusion in Ti-HEA. (a) HAADF image of a selected area in Ti-HEA. (b) The EELS mapping of each element. (c) Line scanning of C, N, and O extracted from the EELS mapping.

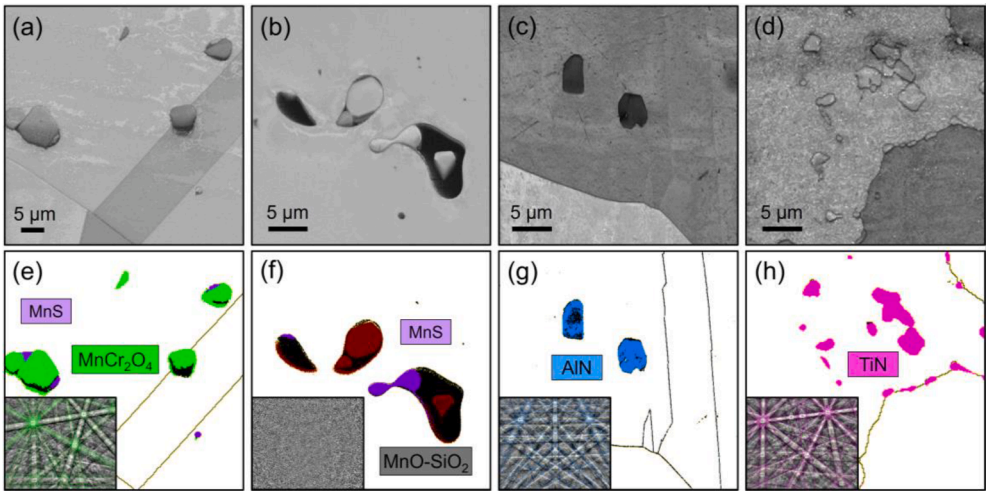

Fig. 9. EBSD identifications of inclusions in HEAs. (a-d) Band maps of O-HEA, Si-HEA, Al-HEA, and Ti-HEA, respectively. (e-h) Phase map and inclusion Kikuchi patterns of O-HEA, Si-HEA, Al-HEA, and Ti-HEA, respectively.

$$\frac{4}{3}Al + O_2 = \frac{2}{3}Al_2O_3 \tag{13}$$

The oxidations of Al, Ti, and other matrix elements were calculated following the most thermodynamically-favored reactions. The formation of $MnCr_2O_4$ was often considered through a two-step process [62], which is summarized in Eqs. (8)–(10). When assuming that the proportion of oxygen and nitrogen is similar to what they are in the air that corresponds to moderate metallurgical and thermal processing conditions (Fig. 1a), the formation of Si_3N_4, TiN, and AlN can be expressed by Eqs. (13)–(15).

$$6Si + 4N_2 = 2Si_3N_4 \tag{13}$$

$$8Al + 4N_2 = 8AlN \tag{14}$$

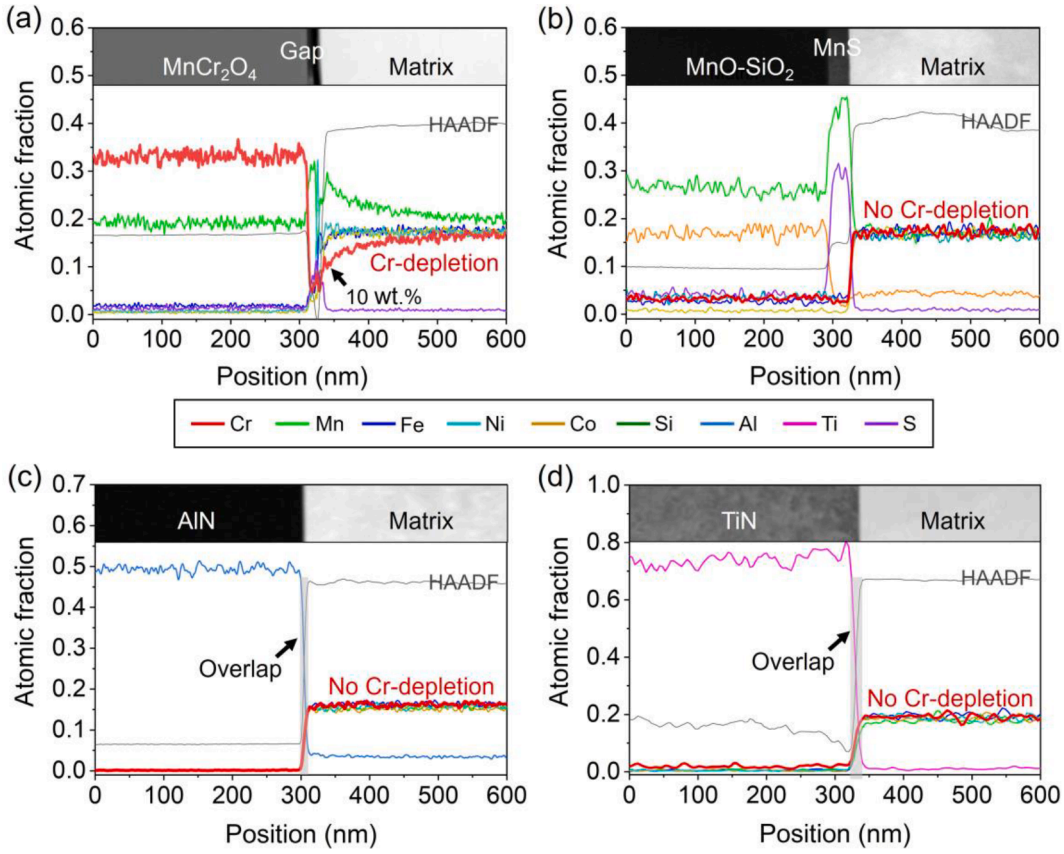

Fig. 10. EDS Line profiles across inclusion-matrix interfaces in different HEAs. (a) O-HEA, (b) Si-HEA, (c) Al-HEA, and (d) Ti-HEA.

$$8Ti + 4N_2 = 8TiN \quad (15)$$

Based on the above reaction coefficients, we plot an integrated Ellingham diagram that comprises the reactions of metals with oxygen and nitrogen, as shown in Fig. 13.

In general, the lower a metal's line is positioned in the Ellingham diagram, the more stable its oxide is. Clearly, the values of ΔG_{SiO_2}, the assumed $\Delta G_{Al_2O_3}$ and ΔG_{TiO_2} are more negative than those of $\Delta G_{Cr_2O_3}$ and $\Delta G_{MnCr_2O_4}$ at all temperatures. As a result, the driving forces for the formation of SiO_2, Al_2O_3, and TiO_2 are stronger than those of Cr-based oxides, thereby preventing the Cr diffusion and the generation of Cr-depletion (Fig. 10) during solidification and thermal processing [12]. On the other hand, the alloy-making processes, such as casting and forging, were conducted under ordinary vacuum conditions (Fig. 1), which means the atmosphere contains both oxygen and nitrogen. In the diagram (Fig. 13), $\Delta G_{Si_3N_4}$ is more positive than ΔG_{SiO_2} at high temperatures, whereas ΔG_{TiN} and ΔG_{AlN} is more negative than $\Delta G_{Al_2O_3}$ and ΔG_{TiO_2}, respectively. In contrast to the formation of oxides in Si-HEA, the observed nitrides in Al-HEA and Ti-HEA are well explained by the calculations. Importantly, the values of ΔG_{TiN} and ΔG_{AlN} are far more negative than the free energies of oxides including the original $MnCr_2O_4$, and therefore, the driving force for related inclusions can finally summarized as: TiN > AlN > SiO_2 > $MnCr_2O_4$. The results also provide a good understanding of the different inclusion amounts (Fig. 2b) and corrosion-resistant enhancements (Fig. 11) observed in the four HEAs. For other alloying elements, it is evident that the oxides of NiO, FeO, and CoO have the most positive free energies, corresponding to the few concentrations of Ni, Fe, and Co found in the oxide inclusions of all HEAs.

As aforementioned, the spinel oxide $MnCr_2O_4$ is the failure mechanism (Fig. 11) that impairs the corrosion resistance of CoCrFeMnNi by forming a Cr-depletion zone adjacent to the inclusion. It is possible to hamper the formation of the crucial Cr_2O_3 by using high-vacuum devices to produce raw materials and the alloy [31]. However, this is challenging for industrial production and would significantly increase costs. We further plotted the relationship between oxygen partial pressure (p_{O_2}) and temperature (Fig. 13) based on the calculations from Eq. (3). Due to the high affinity of Cr and Mn to oxygen, for instance, the thermodynamical prevention of Cr_2O_3 at 1200 °C requires an atmosphere with a p_{O_2} below 1.58×10^{-18}, which is extremely rigorous for metallurgical furnaces. In contrast, the critical p_{O_2} for the oxidation of Si is 9.58×10^{-24} at 1200 °C. Obviously, it is easier to suppress Cr_2O_3 formation by adding Si than by increasing the vacuum degree to such a high level. Hence, we conclude that the addition of Si among the three additives is a simple and cost-effective method that also can avoid the formation of nitride by-products.

4.3. Alloy design for preventing Cr-depletion

In spite of the diverse formation mechanisms and pathways of Cr-based inclusions in specific corrosion-resistant alloys, we surmise that preventing Cr diffusion into oxides is crucial to suppress Cr depletion, which can be achieved by doping other elements with similar functions to the additives in the present study. When $\Delta G_{Cr_2O_3}$ is set as a baseline (Fig. 14a), the oxygen-abhorrent elements with lower oxygen affinity than Cr should comprise Ni, Co, Fe, and Cu. Likewise, the oxygen-preferred elements with higher oxygen affinity than Cr should not be confined to Si, Al, and Ti but also extend to V and rare earths such as La, Ce, Sc, and Y [63–67]. Similar to Mn, the elements of Mg and Ca, albeit with higher oxygen affinity than Cr and often used in ferrous process metallurgy [37], are not recommended as they are not exclusive and thermodynamically favored to form AB_2O_4-type with Cr [68–70]. Therefore, our proposed "inclusion engineering" can be described as follows. For developing alloys with oxygen-abhorrent elements as

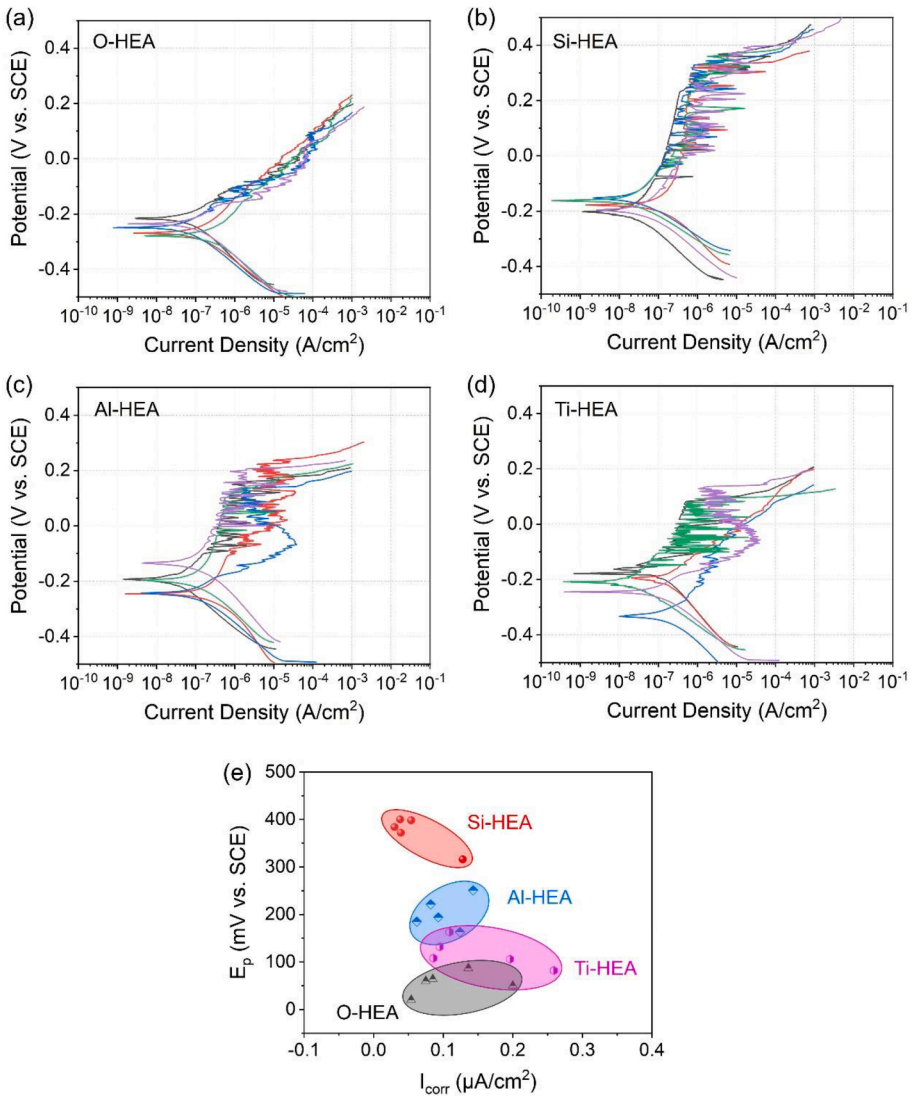

Fig. 11. Passivation behaviors of all alloys using potentiodynamic polarization. (a) O-HEA. (b) Si-HEA. (c) Al-HEA. (d) Ti-HEA. (e) A summary of E_p and I_{corr} of HEAs.

principal components (Fig. 14b), such as Cu-based, Co-based, Ni-based, and Fe-based alloys, we suggest adding a few oxygen-preferred elements since the Cr-based oxides tend to form. In contrast, there is no need to introduce oxygen-preferred elements into alloys with them as principal components, such as V-based alloys, and Cr tends to remain in the matrix.

Here, we show two examples based on this proposed "inclusion engineering". Different from the four HEAs using commercial casting and forging, three alloys, i.e., Ni-based alloys (nominally Ni-20Cr20Mn and Ni-20Cr20Mn2Si, wt. %) and V-based alloys (V-20Cr20Mn, wt. %), were prepared using arc melting furnace. To investigate the Cr-depletion formed during solidification, thermal homogenization was not conducted. As a result, the elemental distributions on a macroscopic scale may not be uniform.

In the first example, TEM-EDS analysis (Figs. 15 and 16) shows that the dominant inclusions in the original Ni-based and Si-modified Ni-based alloys are chromite-type spinel $MnCr_2O_4$ (Fig. 15a and S5a) and amorphous MnO-SiO_2 (Figs. 16a and S5b), respectively, which are similar to those in O-HEA and Si-HEA. Both oxides likely formed in solidification during arc melting [21] since no extra thermal processes were conducted. After adding Si, the Cr-depletion zone is removed in the new alloy, which is revealed by comparing EDS line-scanning profiles (Figs. 15c and 16c). Similar $MnCr_2O_4$ [39] was also found in a Co-based duplex entropic alloy produced using an arc melting furnace. Although the present work did not investigate the Cr distribution at the oxide-matrix interface, the Cr-based oxides implied the Cr-depletion formation and potentially harmful effects on corrosion resistance. Even the $Cr_{40}Co_{40}Ni_{20}$ alloy with a high Cr content suffered from severe anti-corrosion degradation when considerable Cr-depletion zones formed around Cr-rich oxides during thermal spraying under moderate vacuum conditions [27]. Our results indicate that such Cr-depletion can be prevented by doping the proposed oxygen-preferred elements and Si-alloying has been successfully employed in developing other stainless steel with superior corrosion resistance [71].

Another example is the V-based alloy that contains the oxygen-preferred element of V as the principal component (Fig. 14a). As anticipated, the oxide inclusion is rich in V but nearly absent of Cr (Fig. 17c and S6). From TEM identification, the V-based oxide is eventually determined to be MnV_2O_4 (PDF#00-039-0038) with parameter a = 8.53 Å. The results show that Cr assumed in the Cr_2O_3 oxide is replaced by V since $\Delta G_{V_2O_3}$ (−503 kJ/mol O_2) for consuming one mole of oxygen is more negative than $\Delta G_{Cr_2O_3}$(−435 kJ/mol O_2) during solidification, i.e., 1600 °C. As a result, no Cr-depletion is generated in the vicinity of V-rich oxide. Therefore, the three newly developed alloys provide strong evidence that the proposed "inclusion engineering" can be applied in developing other alloys prepared using different

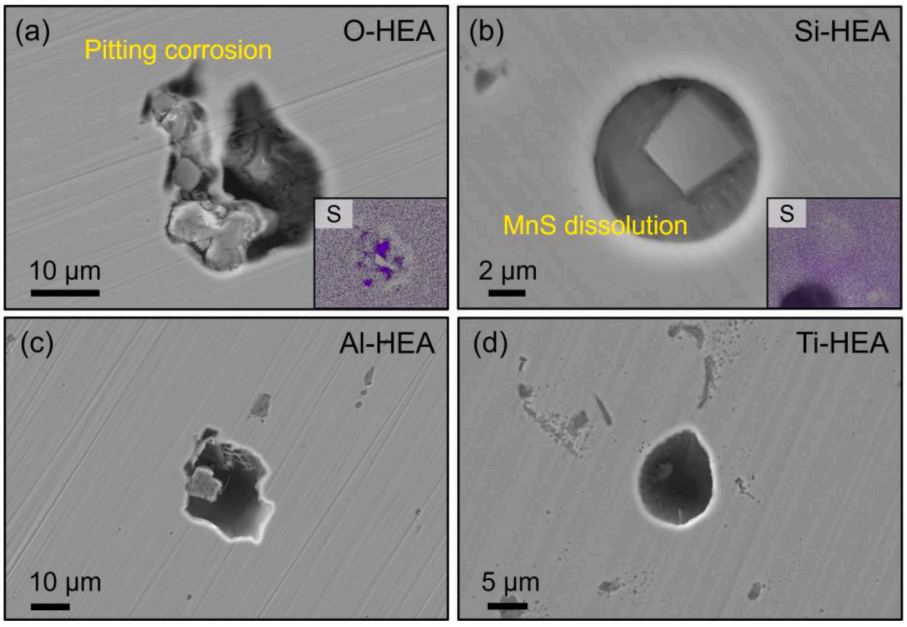

Fig. 12. (a) Inclusion in O-HEA subjected to corrosion and interrupted at 200 mV. (b) Inclusion in Si-HEA subjected to corrosion and interrupted at 200 mV. (c) Typical pit in Al-HEA after corrosion testing at 1 mA/cm^2. (d) Typical pit in Ti-HEA after corrosion testing at 1 mA/cm^2.

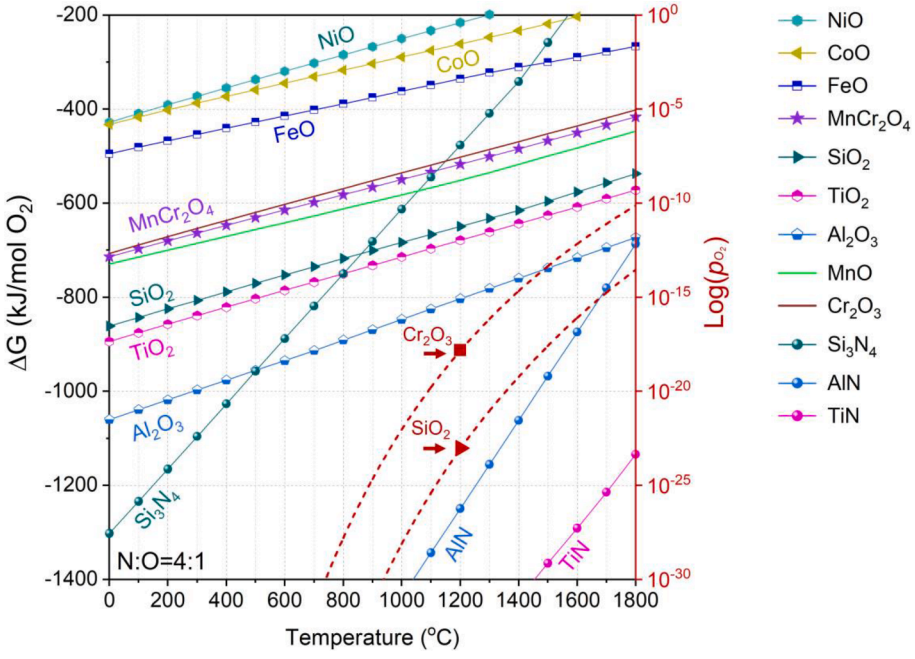

Fig. 13. The integrated Ellingham diagram for the formation of selected oxides and nitrides based on the Gibbs free energies of corresponding reactions over temperatures. The right Y-axis demonstrates the relationship between oxygen partial pressure and temperature.

metallurgical techniques. Oxidation-induced nanoscale Cr-depletion is a pervasive problem that degrades corrosion-resistant alloys. Our strategy also provides a promising solution in alloy design to prevent such degradation.

5. Conclusions

The inclusions, surrounding Cr distributions, and corrosion resistance of the original, Si-modified, Al-modified, and Ti-modified CoCrFeMnNi high entropy alloys are studied and compared. An effective strategy based on "inclusion engineering" is proposed for designing corrosion-resistant alloys to prevent Cr-depletion. The main findings are:

1. The dominant inclusions in the original, Si-modified, Al-modified, and Ti-modified CoCrFeMnNi alloys are $MnCr_2O_4$, MnO-SiO_2, AlN, and TiN, respectively. Nanoscale Cr-depletion with 150–200 nm forms in the original alloy but is retarded in the modified alloys due to the prevention of Cr diffusion.
2. After eliminating Cr-depletion by Si, Al, and Ti, the corrosion resistance of all the modified alloys is improved at different levels. The enhancement from Si addition is the best, followed by Al and Ti. The inferior enhancements from Al and Ti are attributed to the large-

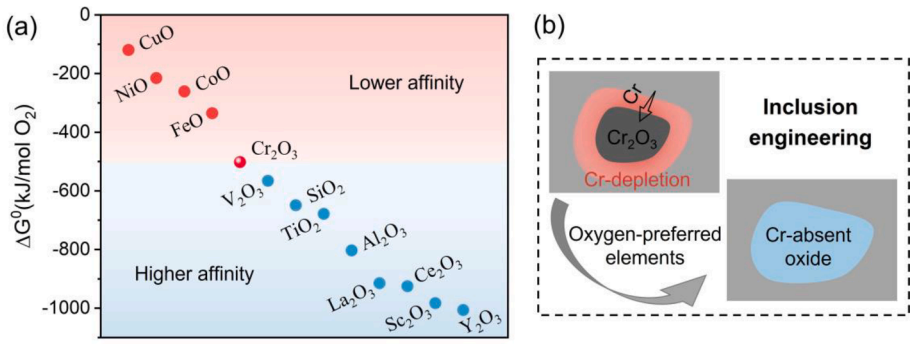

Fig. 14. Anti-corrosion alloy development by inclusion engineering. (a) Standard Gibbs formation energies of the selected oxides at 1200 °C. (b) a schematic diagram of the proposed inclusion engineering.

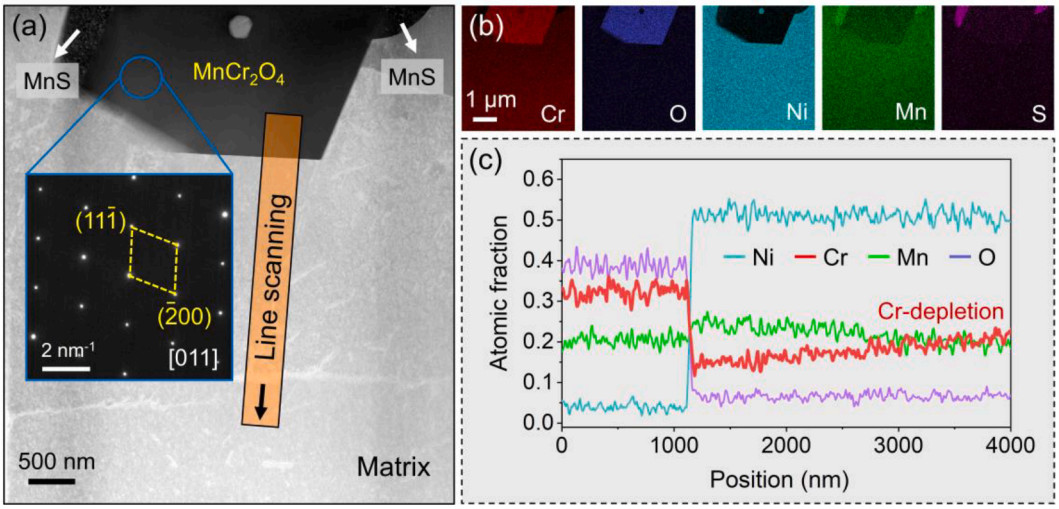

Fig. 15. Identification of the inclusions in the original Ni-based alloy. (a) HAADF image of the inclusion with insert SAED indicating its structure. (b) TEM-EDS mapping of the inclusion. (c) EDS elemental line profiles across the inclusion-matrix interface.

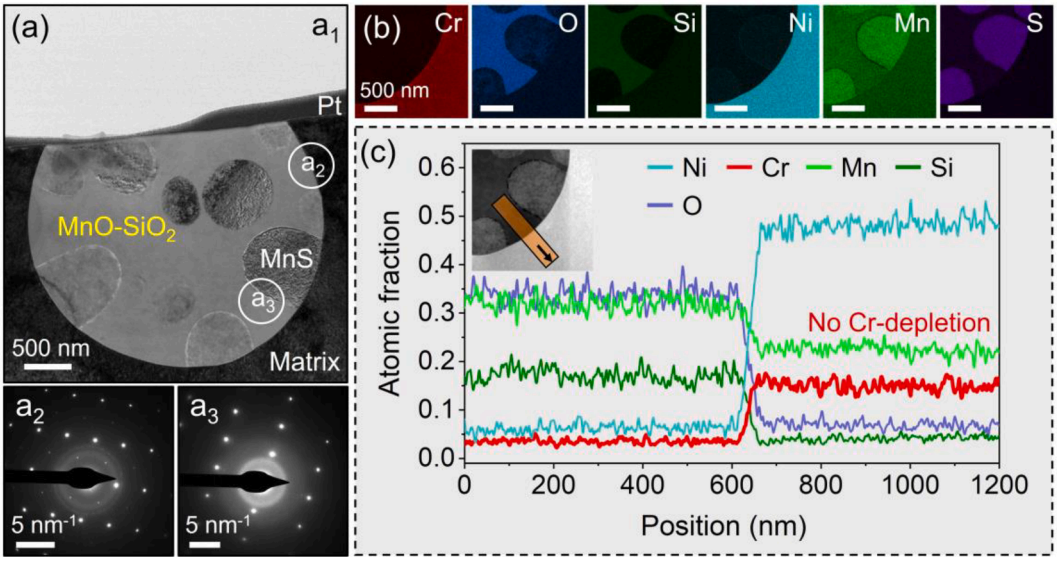

Fig. 16. Identification of the inclusions in the Si-modified Ni-based alloy. (a) Microstructure identification of the inclusions in the Si-modified Ni-based alloy. (a_1) TEM image of the inclusion; (a_2) SAED of the area a_2 in a_1; (a_3) SAED of the area a_3 in a_1. (b) HAADF-EDS mapping of the inclusion. (c) EDS elemental line profiles across the inclusion-matrix interface.

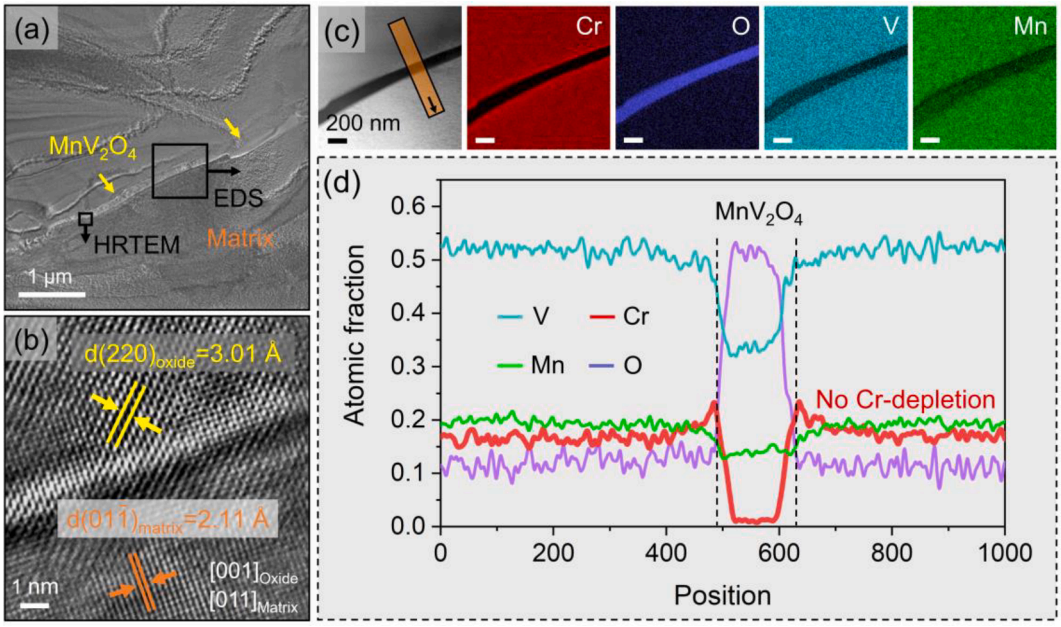

Fig. 17. Identification of the inclusions in the V-based alloy. (a) TEM image of the inclusions in the V-based alloy without doping other oxygen-preferred elements. (b) HRTEM image of inclusion-matrix interface. (c) HAADF-EDS mapping of the inclusion. (d) EDS elemental line profiles across the inclusion-matrix interface.

scale formation of AlN and TiN by-products with area ratios estimated at 1 % and 3 %, respectively.

3. Calculating Gibbs free energy changes provides a thermodynamic foundation for inclusion modification and details the associated risk. Si, Al, and Ti all have a stronger oxygen affinity than Cr, clarifying the removal of Cr-depletion. However, the nitridations of Al and Ti are preferential to occur than their oxidations in a moderate vacuum condition.
4. To prevent potential Cr-depletion, the oxygen-preferred elements are recommended in the development of corrosion-resistant alloys based on Fe, Cu, Ni, and Co. In contrast, no additional elements are required in V-based alloys as oxidation-induced Cr diffusion is prevented by V.

CRediT authorship contribution statement

K.P. Yu: Writing – original draft, Validation, Methodology, Investigation, Formal analysis, Data curation, Conceptualization. **H. Jiang:** Investigation, Formal analysis, Data curation. **X.Y. Xu:** Investigation, Formal analysis, Data curation. **M.X. Huang:** Writing – review & editing, Validation, Supervision, Resources, Project administration, Investigation, Funding acquisition, Formal analysis, Conceptualization.

Declaration of competing interest

The authors declare that they have no known competing financial interests or personal relationships that could have appeared to influence the work reported in this paper.

Data availability

Data will be made available on request.

Acknowledgments

M.X. Huang acknowledges the financial support from the National Key Research and Development Program of China (No.2019YFA0209900), National Natural Science Foundation of China (No. 52130102), Research Grants Council of Hong Kong (No. 17307123, C7045-19E), and New Cornerstone Science Foundation through the XPLORER PRIZE.

Appendix A. Supplementary data

Supplementary data to this article can be found online at https://doi.org/10.1016/j.matdes.2024.113146.

References

[1] H.M. Cobb, The history of stainless steel, ASM International (2010).
[2] A. Brooks, C. Clayton, K. Doss, Y. Lu, On the role of Cr in the passivity of stainless steel, J. Electrochem. Soc. 133 (12) (1986) 2459.
[3] C. Liu, J. Wu, Influence of pH on the passivation behavior of 254SMO stainless steel in 3.5% NaCl solution, Corros. Sci. 49 (5) (2007) 2198–2209.
[4] A.C. Lloyd, J.J. Noel, S. Mcintyre, D.W. Shoesmith, Cr, Mo and W alloying additions in Ni and their effect on passivity, Electrochim. Acta 49 (2004) 3015–3027.
[5] B. Yang, J. Li, X. Gong, Y. Nie, Y. Li, Effects of Cu addition on the corrosion behavior of NiCoCrMo alloys in neutral chloride solution, RSC Adv. 7 (65) (2017) 40779–40790.
[6] A.Y. Gerard, J. Han, S.J. McDonnell, K. Ogle, E.J. Kautz, D.K. Schreiber, P. Lu, J. E. Saal, G.S. Frankel, J.R. Scully, Aqueous passivation of multi-principal element alloy Ni38Fe20Cr22Mn10Co10: Unexpected high Cr enrichment within the passive film, Acta Mater. 198 (2020) 121–133.
[7] H. Feng, H. Li, X. Wu, Z. Jiang, S. Zhao, T. Zhang, D. Xu, S. Zhang, H. Zhu, B. Zhang, Effect of nitrogen on corrosion behaviour of a novel high nitrogen medium-entropy alloy CrCoNiN manufactured by pressurized metallurgy, J. Mater. Sci. Technol. 34 (10) (2018) 1781–1790.
[8] A.Y. Gerard, E.J. Kautz, D.K. Schreiber, J. Han, S. McDonnell, K. Ogle, P. Lu, J.E. Saal, G.S. Frankel, J.R. Scully, The role of chromium content in aqueous passivation of a non-equiatomic Ni38Fe20CrxMn21-0.5 xCo21-0.5 x multi-principal element alloy (x= 22, 14, 10, 6 at%) in acidic chloride solution, Acta Mater. 245 (2023) 118607.
[9] Y. Xie, D.M. Artymowicz, P.P. Lopes, A. Aiello, D. Wang, J.L. Hart, E. Anber, M. L. Taheri, H. Zhuang, R.C. Newman, A percolation theory for designing corrosion-resistant alloys, Nat. Mater. 20 (6) (2021) 789–793.
[10] P. Brüesch, K. Müller, A. Atrens, H. Neff, Corrosion of stainless steels in chloride solution: an XPS investigation of passive films, Appl. Phys. A 38 (1985) 1–18.
[11] K. Asami, K. Hashimoto, S. Shimodaira, An XPS study of the passivity of a series of iron—chromium alloys in sulphuric acid, Corros. Sci. 18 (2) (1978) 151–160.
[12] C. Zhang, K.C. Chan, Y. Wu, L. Liu, Pitting initiation in Fe-based amorphous coatings, Acta Mater. 60 (10) (2012) 4152–4159.
[13] K. Yu, S. Feng, D. Chao, P. Yu, M. Huang, Improving anti-corrosion properties of CoCrFeMnNi high entropy alloy by introducing Si into nonmetallic inclusions, Corros. Sci. (2022) 110616.
[14] M.P. Ryan, D.E. Williams, R.J. Chater, B.M. Hutton, D.S. Mcphail, Why stainless steel corrodes, Nature 415 (6873) (2002) 770–774.

[15] D.E. Williams, Y.Y. Zhu, Explanation for initiation of pitting corrosion of stainless steels at sulfide inclusions, J. Electrochem. Soc. 147 (5) (2000) 1763.
[16] C. Kovach, R. Wells, A. Moskowitz, The sulfide phases in iron-chromium steels, ASM Trans. Q. 61 (3) (1968) 575–581.
[17] E.G. Webb, R.C. Alkire, Pit initiation at single sulfide inclusions in stainless steel: I. Electrochemical microcell measurements, J. Electrochem. Soc. 149 (6) (2002) B272.
[18] H. Krawiec, V. Vignal, O. Heintz, R. Oltra, Influence of the dissolution of MnS inclusions under free corrosion and potentiostatic conditions on the composition of passive films and the electrochemical behaviour of stainless steels, Electrochim. Acta 51 (16) (2006) 3235–3243.
[19] P. Schmuki, H. Hildebrand, A. Friedrich, S. Virtanen, The composition of the boundary region of MnS inclusions in stainless steel and its relevance in triggering pitting corrosion, Corros. Sci. 47 (5) (2005) 1239–1250.
[20] J.H. Park, Y. Kang, Inclusions in stainless steels – a review, Steel Res. Int. 88(12) (2017) 1700130.
[21] K. Volenık, F. Hanousek, P. Chraska, J. Ilavský, K. Neufuss, In-flight oxidation of high-alloy steels during plasma spraying, Mater. Sci. Eng. A 272 (1) (1999) 199–206.
[22] J.-H. Shim, Y.-J. Oh, J.-Y. Suh, Y. Cho, J.-D. Shim, J.-S. Byun, D. Lee, Ferrite nucleation potency of non-metallic inclusions in medium carbon steels, Acta Mater. 49 (12) (2001) 2115–2122.
[23] X. Yang, F. Tang, X. Hao, Z. Li, Oxide evolution during the solidification of 316L stainless steel from additive manufacturing powders with different oxygen contents, Metall. Mater. Trans. B 52 (4) (2021) 2253–2262.
[24] Z. Shen, K. Chen, H. Yu, B. Jenkins, Y. Ren, N. Saravanan, G. He, X. Luo, P.A. Bagot, M.P. Moody, New insights into the oxidation mechanisms of a Ferritic-Martensitic steel in high-temperature steam, Acta Mater. 194 (2020) 522–539.
[25] C. Mennicke, M.-Y. He, D. Clarke, J. Smith, The role of secondary oxide inclusions ("pegs") on the spalling resistance of oxide films, Acta Mater. 48 (11) (2000) 2941–2949.
[26] J. Wu, S. Zhang, W. Sun, Y. Gao, J. Wang, Enhanced corrosion resistance in Fe-based amorphous coatings through eliminating Cr-depleted zones, Corros. Sci. 136 (2018) 161–173.
[27] G. Koga, A. Nascimento, F. Ettouil, L. Rodrigues, G. Zepon, C. Bolfarini, C. Kiminami, W. Botta, R. Schulz, A.C. e Silva, Thermally sprayed multi-principal element Cr40Co40Ni20 coatings–Oxidation upon coatings' build-up and electrochemical corrosion, Surf. Coat. Technol. 454 (2023) 129154.
[28] K. Park, H. Kwon, Effects of Mn on the localized corrosion behavior of Fe–18Cr alloys, Electrochim. Acta 55 (9) (2010) 3421–3427.
[29] S. Zheng, Y. Wang, B. Zhang, Y. Zhu, C. Liu, P. Hu, X. Ma, Identification of MnCr2O4 nano-octahedron in catalysing pitting corrosion of austenitic stainless steels, Acta Mater. 58 (15) (2010) 5070–5085.
[30] H.-Y. Ha, M.-H. Jang, T.-H. Lee, Influences of Mn in solid solution on the pitting corrosion behaviour of Fe-23 wt% Cr-based alloys, Electrochim. Acta 191 (2016) 864–875.
[31] J. Pang, T. Xiong, X. Wei, Z. Zhu, B. Zhang, Y. Zhou, X. Shao, Q. Jin, S. Zheng, X. Ma, Oxide MnCr2O4 induced pitting corrosion in high entropy alloy CrMnFeCoNi, Materialia 6 (2019) 100275.
[32] M. Barbosa, The pitting resistance of AISI 316 stainless steel passivated in diluted nitric acid, Corros. Sci. 23 (12) (1983) 1293–1305.
[33] J. Noh, N. Laycock, W. Gao, D. Wells, Effects of nitric acid passivation on the pitting resistance of 316 stainless steel, Corros. Sci. 42 (12) (2000) 2069–2084.
[34] N. Hara, K. Hirabayashi, Y. Sugawara, I. Muto, Improvement of pitting corrosion resistance of type 316L stainless steel by potentiostatic removal of surface MnS inclusions, Int. J. Corros. 2012 (2012).
[35] L. Pao, I. Muto, Y. Sugawara, Pitting at inclusions of the equiatomic CoCrFeMnNi alloy and improving corrosion resistance by potentiodynamic polarization in H2SO4, Corros. Sci. 191 (2021) 109748.
[36] I.-H. Jung, S.A. Decterov, A.D. Pelton, Computer applications of thermodynamic databases to inclusion engineering, ISIJ Int. 44 (3) (2004) 527–536.
[37] L. Holappa, O. Wijk, Inclusion engineering, Treat. Process Metall. (2014) 347–372.
[38] A. Slagter, J. Everaerts, L. Deillon, A. Mortensen, Strong silicon oxide inclusions in iron, Acta Mater. 242 (2023) 118437.
[39] W. Wang, Y. Wang, W. Mu, J.H. Park, H. Kong, S. Sukenaga, H. Shibata, H. Larsson, H. Mao, Inclusion engineering in Co-based duplex entropic alloys, Mater. Des. 210 (2021) 110097.
[40] J.M. Park, J. Choe, J.G. Kim, J.W. Bae, J. Moon, S. Yang, K.T. Kim, J.-H. Yu, H. S. Kim, Superior tensile properties of 1% C-CoCrFeMnNi high-entropy alloy additively manufactured by selective laser melting, Mater. Res. Lett. 8 (1) (2020) 1–7.
[41] C. Man, C. Dong, K. Xiao, Q. Yu, X. Li, The combined effect of chemical and structural factors on pitting corrosion induced by MnS-(Cr, Mn, Al) O duplex inclusions, Corrosion 74 (3) (2018) 312–325.
[42] Iso, Method of measuring the pitting potential for stainless steels by potentiodynamic control in sodium chloride solution, ISO (2014) 15158.
[43] B. Zhang, X. Ma, A review—Pitting corrosion initiation investigated by TEM, J. Mater. Sci. Technol. 35 (7) (2019) 1455–1465.
[44] Y. Ren, L. Zhang, P.C. Pistorius, Transformation of oxide inclusions in type 304 stainless steels during heat treatment, Metall. Mater. Trans. B 48 (5) (2017) 2281–2292.
[45] H. Ohta, H. Suito, Precipitation and dispersion control of MnS by deoxidation products of ZrO2, Al2O3, MgO and MnO–SiO2 particles in Fe–10mass% Ni alloy, ISIJ Int. 46 (4) (2006) 480–489.
[46] J. Fu, W. Qiu, Q. Nie, Y. Wu, Precipitation of TiN during solidification of AISI 439 stainless steel, J. Alloy. Compd. 699 (2017) 938–946.
[47] G. Tirumalasetty, M. Van Huis, C. Fang, Q. Xu, F. Tichelaar, D. Hanlon, J. Sietsma, H. Zandbergen, Characterization of NbC and (Nb, Ti) N nanoprecipitates in TRIP assisted multiphase steels, Acta Mater. 59 (19) (2011) 7406–7415.
[48] Y. Zhao, W. Liu, T. Zhang, Z. Sun, Y. Wang, Y. Fan, B. Dong, Assessment of the correlation between M23C6 precipitates and pitting corrosion resistance of 0Cr13 martensitic stainless steel, Corros. Sci. 189 (2021) 109580.
[49] H. Feng, H.-B. Li, J. Dai, Y. Han, J.-D. Qu, Z.-H. Jiang, Y. Zhao, T. Zhang, Why CoCrFeMnNi HEA could not passivate in chloride solution?–A novel strategy to significantly improve corrosion resistance of CoCrFeMnNi HEA by N-alloying, Corros. Sci. 204 (2022) 110396.
[50] Y. Zhao, M. Wang, H. Cui, Y. Zhao, X. Song, Y. Zeng, X. Gao, F. Lu, C. Wang, Q. Song, Effects of Ti-to-Al ratios on the phases, microstructures, mechanical properties, and corrosion resistance of Al2-xCoCrFeNiTix high-entropy alloys, J. Alloy. Compd. 805 (2019) 585–596.
[51] Z. Han, N. Chen, S. Lu, H. Luan, R. Peng, H. Xu, Y. Shao, Z. Peng, K. Yao, Structures and corrosion properties of the AlCrFeNiMo0. 5Tix high entropy alloys, Mater. Corros. 69 (5) (2018) 641–647.
[52] Y.-J. Hsu, W.-C. Chiang, J.-K. Wu, Corrosion behavior of FeCoNiCrCux high-entropy alloys in 3.5% sodium chloride solution, Mater. Chem. Phys. 92 (1) (2005) 112–117.
[53] Y. Yi, P. Cho, A. Al Zaabi, Y. Addad, C. Jang, Potentiodynamic polarization behaviour of AISI type 316 stainless steel in NaCl solution, Corros. Sci. 74 (2013) 92–97.
[54] Z. Li, X. Ding, L. Chen, J. He, J. Chen, J. Chen, N. Hua, P. Dai, Q. Tang, Effect of Si content and annealing temperatures on microstructure, tensile properties of FeCoCrNiMn high entropy alloys, J. Alloy. Compd. 935 (2023) 168090.
[55] D. Wei, W. Gong, T. Tsuru, I. Lobzenko, X. Li, S. Harjo, T. Kawasaki, H.-S. Do, J. W. Bae, C. Wagner, Si-addition contributes to overcoming the strength-ductility trade-off in high-entropy alloys, Int. J. Plast 159 (2022) 103443.
[56] J. Kumar, A. Linda, M. Sadhasivam, K. Pradeep, N. Gurao, K. Biswas, The effect of Si addition on the structure and mechanical properties of equiatomic CoCrFeMnNi high entropy alloy by experiment and simulation, Materialia 27 (2023) 101707.
[57] P. Wu, Y. Zhang, L. Han, K. Gan, D. Yan, W. Wu, L. He, Z. Fu, Z. Li, Unexpected sluggish martensitic transformation in a strong and super-ductile high-entropy alloy of ultralow stacking fault energy, Acta Mater. 261 (2023) 119389.
[58] B. Ren, R.-F. Zhao, Z.-X. Liu, S.-K. Guan, H.-S. Zhang, Microstructure and properties of Al 0.3 CrFe 1.5 MnNi 0.5 Ti x and Al 0.3 CrFe 1.5 MnNi 0.5 Si x high-entropy alloys, Rare Met. 33 (2) (2014) 149–154.
[59] Y. Shi, B. Yang, X. Xie, J. Brechtl, K.A. Dahmen, P.K. Liaw, Corrosion of AlxCoCrFeNi high-entropy alloys: Al-content and potential scan-rate dependent pitting behavior, Corros. Sci. 119 (2017) 33–45.
[60] Y. Chen, T. Duval, U. Hung, J. Yeh, H. Shih, Microstructure and electrochemical properties of high entropy alloys—a comparison with type-304 stainless steel, Corros. Sci. 47 (9) (2005) 2257–2279.
[61] H. Wang, W. Wang, Precipitation of complex carbonitrides in a Nb–Ti microalloyed plate steel, J. Mater. Sci. 44 (2) (2009) 591–600.
[62] I. Saeki, H. Konno, R. Furuichi, T. Nakamura, K. Mabuchi, M. Itoh, The effect of the oxidation atmosphere on the initial oxidation of type 430 stainless steel at 1273 K, Corros. Sci. 40 (2–3) (1998) 191–200.
[63] R. Geng, J. Li, C. Shi, J. Zhi, B. Lu, Effect of Ce-La on inclusion evolution in Al-killed high strength steel, Metall. Res. Technol. 117 (6) (2020) 616.
[64] Z. Adabavazeh, W. Hwang, Y. Su, Effect of adding cerium on microstructure and morphology of Ce-based inclusions formed in low-carbon steel, Sci. Rep. 7 (1) (2017) 46503.
[65] H. Torkamani, S. Raygan, C. Garcia Mateo, J. Rassizadehghani, J. Vivas, Y. Palizdar, D. San-Martin, The influence of La and Ce addition on inclusion modification in cast niobium microalloyed steels, Metals 7 (9) (2017) 377.
[66] B. Li, H. Zhu, J. Zhao, M. Song, J. Li, Z. Xue, Effect of rare-earth La on inclusion evolution in high-Al steel, Steel Res. Int. 93 (2) (2022) 2100347.
[67] Y. Wu, Y. Li, Y. Xu, M. Kang, J. Wang, B. Sun, Unveiling the mechanism of yttrium-related microstructure inhibiting or promoting high-temperature oxidation based on Ni-Al-Y alloys, Acta Mater. 211 (2021) 116879.
[68] L. Cheng, L. Zhang, Y. Ren, J. Zhang, Wettability and interfacial behavior between cerium containing stainless steel and MgO–Cr2O3-based lining refractory, J. Alloy. Compd. 845 (2020) 155877.
[69] T. Itoh, T. Nagasaka, M. Hino, Equilibrium between dissolved chromium and oxygen in liquid high chromium alloyed steel saturated with pure Cr2O3, ISIJ Int. 40 (11) (2000) 1051–1058.
[70] H. Li, Y. Zheng, L.W. Benum, M. Oballa, W. Chen, Carburization behaviour of Mn–Cr–O spinel in high temperature hydrocarbon cracking environment, Corros. Sci. 51 (10) (2009) 2336–2341.
[71] K. Yu, S. Feng, C. Ding, M. Gu, P. Yu, M. Huang, A sequential dual-passivation strategy for designing stainless steel used above water oxidation, Mater. Today 70 (2023) 8–16.